PCCP

PAPER

View Article Online
View Journal | View Issue

Cite this: *Phys. Chem. Chem. Phys.*, 2025, **27**, 14305

Understanding electrochemical reactions using density functional theory: the bridging theoretical scheme of squares and experimental cyclic voltammetry†

Amir Mahdian, Arsalan Hashemi and Kari Laasonen *

Received 16th April 2025,
Accepted 8th June 2025

DOI: 10.1039/d5cp01464f

rsc.li/pccp

Mechanistic redox and acid–base reactions play pivotal roles in numerous applications in both chemistry and biology. Bridging the gap between computational insights and experimental observations is crucial to illuminate the mechanisms underlying these redox processes. In this study, we investigate electrochemical reactions by using the scheme of squares framework for a set of tens of molecules that have been examined for redox flow batteries. Furthermore, we focused on developing our computational models by calibrating the calculated redox potentials against experimental data, thereby enhancing the predictive accuracy of our approach. These findings are relevant across a wide range of applications from energy storage to medicine and synthetic chemistry.

1. Introduction

The study of electron and proton transfer and its role in chemical reactions is fundamental to the functionality of various electrochemical devices including batteries, fuel cells, and electrolysis systems.[1–6] To enhance the performance of these applications, a thorough understanding of the energy pathways within the reaction mechanism is required. Accordingly, both kinetics and thermodynamics analyses are essential for assessing electrochemical reactions.[7,8]

In flow batteries,[9,10] reversible electrochemical reactions are essential for facilitating successful charging and discharging. Full reversibility occurs when electrons move back and force between an electrode and a redox-active molecule in a potential cycle. This means that any additional reactions consuming electrons[11] must be minimal. An acid–base reaction,[12] disproportionation,[13] electrode passivation,[14] and molecule decomposition[15] are examples of chemical reactions, which add complexity to the mechanism of electron transfer and potentially introducing irreversibility into the desired redox reaction. Of these reactions, the acid–base reaction is a relatively simple reaction where an acid donates a proton (H^+) to a base, forming a conjugate base and a conjugate acid. When this reaction takes place alongside the redox reactions, it will alter the overall process.[16] The acid–base reaction is rather easy to model and should be added to the redox potential modelling whereas the other reactions are more difficult to model.

Cyclic voltammetry (CV) is one of the most widely used techniques for characterizing redox-active systems.[17–20] This involves applying a potential to an electrode relative to a fixed reference potential, such as the standard hydrogen electrode (SHE).[21] The potential varies linearly over time within the electrochemical potential window of the electrolyte. As an indicator of the number of electrons transferred, the current is measured simultaneously. Therefore, it is possible to determine the number of oxidation states and their stability, reaction rates, and redox potentials.[22] With common experimental methods, it is challenging to obtain atomic-level details. Consequently, computational analyses are very useful for gaining a deeper understanding of electrochemical properties and redox mechanisms.

Through electrochemical reaction analyses, kinetics assessments, however, require very time consuming computations or model simplification.[23–25] The thermodynamic data are easily evaluated by determining the changes in the Gibbs free energy (ΔG) of the reactants and products which are equivalent to the experimental redox potential obtained from the CV analysis. Therefore, the key is to computationally examine various reaction pathways to determine whether the process involves a decoupled electron transfer (ET) and proton transfer (PT) or a coupled (simultaneous) proton–electron transfer (PET).[26,27] These pathways can be systematically diagrammed along the sides and diagonal of a square, forming a representation known as an electrochemical scheme of squares.[28–30]

The density functional theory (DFT) approach[31,32] in combination with implicit solvation models[33] and a computational

Department of Chemistry and Material Science, School of Chemical Engineering, Aalto University, 02150 Espoo, Finland. E-mail: kari.laasonen@aalto.fi

† Electronic supplementary information (ESI) available. See DOI: https://doi.org/10.1039/d5cp01464f

standard hydrogen electrode (SHE)[34] are frequently used to simulate electrochemical environments. Despite their widespread use, these methods face challenges, including the accurate modeling of charged systems and addressing deficiencies in exchange–correlation (XC) functionals.[35] These limitations can lead to discrepancies, for example, in the Gibbs free energy, compared to the experimental values.[36]

To address this issue, one can scale the DFT results to the corresponding experimental results. This adjustment should eliminate discrepancies and indirectly incorporate the experimental effects into the calculated values. Generally, the validity and diversity of the collected data are crucial. For instance, our group,[37] along with others,[38–40] scaled theoretical pK_a values to match experimental values in various solvents for organic molecules. ET redox potential has also been calibrated to align with experimental values with accuracy as good as about 0.1 V.[41–44] For example, Hamza *et al.*[42] adjusted the redox potential for pyridinium derivatives. These studies focus only on ET whereas we will also include the PET reactions.

In what follows, we explain how the electrochemical scheme of squares can be employed to interpret and predict the experiments. We also scale the redox potentials for both the ET and PET reactions to align with experimental data. To this end, a systematic effort was made to establish a relationship that reconciles the discrepancies between theoretical predictions and experimental measurements. This approach not only deepens our understanding of redox behavior but also establishes a foundational framework for accurately predicting the electrochemical properties of new molecular systems in other related fields of research.

2. Criteria for electrochemical reversibility

2.1. Redox potential

The CV technique measures the relationship between the potential and the current resulting from electrochemical reactions occurring at the working electrode surface. These reactions can be exemplified by the following reduction process:

$$[\text{electrode}]^n + \text{X}^m \rightarrow [\text{electrode}]^{n-n_e} + \text{X}^{m+n_e} \quad (1)$$

In this reaction, n and m represent the numbers of electrons in the electrode and molecule X, respectively. Additionally, n_e represents the number of electrons transferred from the electrode to X during the reduction reaction. A reverse reaction, known as oxidation, can also be considered. During the redox (reduction–oxidation) process, each species may also undergo proton (H^+) transfer reactions:

$$\text{X}^m + n_p\text{H}^+ \rightarrow [\text{XH}_{n_p}]^{m-n_p}. \quad (2)$$

Here, n_p represents the number of protons involved in the acid–base reactions. This reaction may occur sequentially or simultaneously with the ET reaction. The sequence of reactions can vary, and several intermediate states can be formed depending on the number of electrons and protons involved. Fig. 1 illustrates various mechanisms for one-electron, one-proton transfer reactions.

When the electrode potential is applied, the current peaks as a function of the ratio of the activities of the oxidized (ox) and reduced (red) species at the potential E:

$$E = E^0_{\text{ox/red}} + \frac{RT}{n_eF}\ln\left(\frac{a_{\text{ox}}}{a_{\text{red}}}\right). \quad (3)$$

This equation is referred to as the Nernst equation.[45] Here, $E^0_{\text{ox/red}}$ is defined as the standard potential, which is equal for both the reduction and oxidation reactions. The parameter a_i, which denotes the activity of species i, is defined as follows:

$$a_i = \gamma_i\left(\frac{c_i}{c^0_i}\right),$$

where γ_i is a dimensionless activity coefficient, c_i is the concentration of species i near the electrode surface, and c^0 represents the standard concentration. The symbols T, F, and R represent the temperature (in K), the Faraday constant, and the universal ideal gas constant, respectively.

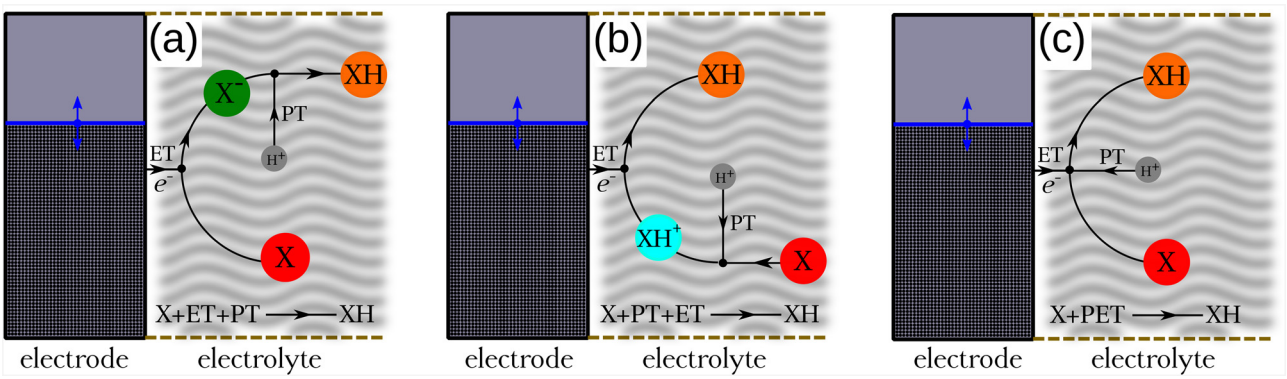

Fig. 1 Schematic representation of the reduction reaction of the molecule X adjacent to an electrode through various mechanisms: X is converted into XH *via* (a) sequential electron transfer (ET) followed by proton transfer (PT), (b) sequential proton transfer (PT) followed by electron transfer (ET), and (c) simultaneous proton–electron transfer (PET) reactions. The electrode energy level (blue line) can be adjusted to source electrons for the favored reaction.

Now, let us examine how different reactions impact E:

PT reaction. The proton is supplied by the solution. The PT reaction thus depends solely on the acidity constant of the active species and pH of solution. This reaction is a chemical reaction and proceeds without any direct electrode involvement.

ET reaction. Assuming a 1 : 1 ratio for the ET reactions (the oxidized and reduced species have the same activity) allows us to disregard the second term of eqn (3), simplifying it to $E = E^0_{ox/red}$ (because $\ln 1 = 0$). $E^0_{ox/red}$ can also be computed with quantum chemistry using the following equation:

$$E^0_{ox/red} = -\frac{\Delta G_{ox/red}}{n_e F} = -\frac{\Delta G_{X^m/X^{m+n_e}}}{n_e F} \quad (4)$$

Here, $\Delta G_{X^m/X^{m+n_e}}$ denotes the change in the Gibbs free energy associated with the different charge states of the molecule. Gibbs free energy of each molecule was computed using quantum chemistry software (Gaussian 16), employing the SMD solvation model to account for solvation effects.

PET reaction. When H^+ ions are also involved in the redox reactions, it becomes crucial to define the formal potential for the overall reaction rather than just for the ET reaction:

$$[\text{electrode}]^n + X^m + n_p H^+ \rightarrow [\text{electrode}]^{n-n_e} + [XH_{n_e}]^{m+n_e-n_p}. \quad (5)$$

In such a reaction, the activity of H^+ is conventionally set to 1 (pH of 0) to determine $E^0_{ox/red}$. Eqn (4) is used again, but in this instance, with $\Delta G_{X^m/[XH_{n_p}]^{m+n_e-n_p}}$. The activity of the H^+ species can be adjusted by the pH of the solution, as described by the following equation:

$$pH = -\log(a_{H^+}) \quad (6)$$

Consequently, the activity a_{H^+} is determined as follows:

$$a_{H^+} = 10^{-pH} \quad (7)$$

In reactions where there are n_p protons involved (as outlined in eqn (5)), the activity ratio can be expressed as follows:

$$\frac{a_{ox}}{a_{red}} = \frac{a_{X^m} \cdot [a_{H^+}]^{n_p}}{a_{[XH_{n_p}]^{m+n_e-n_p}}}, \quad (8)$$

Integrating eqn (3), (7) and (8), the Nernst equation can be reformulated for our specific system as follows:

$$E = E^0_{X^m/[XH_{n_p}]^{m+n_e-n_p}} - \left(\frac{n_p RT \ln(10)}{n_{el} F}\right) pH. \quad (9)$$

At room temperature, the value of $RT\ln(10)/F$ is approximately 0.059 eV.

2.2. Reversible electrochemical reactions using the scheme of squares

The electrochemical reaction will be regarded reversible when oxidation and reduction reactions mirror each other near the $E^0_{ox/red}$. The $E^0_{ox/red}$ is the average of voltage of the anodic and cathodic current peaks. In such cases, the characteristic duck-shaped voltammogram also indicates an absence of degradation reactions during measurements. There can be some electrochemical reactions within the potential scanning window with different $E^{0,n}_{ox/red}$. They will be analysed in a similar manner as a single reaction. If all reactions are reversible, the total potential cycle is reversible. The applied potential has to be limited within the solvent electrochemical potential window (E_w). This is needed to exclude the reactions of the solvent molecules. For aqueous solutions, the E_w value is between −1.5 and +1.5 V_{SHE}.[46]

The irreversibility can be caused by the PT (or PET) reaction. The pK_a 's of a molecule depend strongly on the charge state of it and we can assume that the pH is constant during the potential cycle. At certain voltage, a molecule can get to a protonation state which it cannot return to the earlier state *via* ET or PET, as demonstrated in examples presented later in this manuscript. As we study only a single molecule without changing its backbone connectivity, we cannot address irreversibility by molecule breaking, dimerization or other more complex reactions.

3. Computational frameworks

All DFT calculations were conducted using Gaussian 16 software.[47] Molecular geometry optimizations were conducted using two separate sets of calculations: (i) the 6-31G(d) basis set[48] combined with the M06-2X functional[48] and (ii) the PM7 semiempirical method,[49] both of which incorporate the SMD solvation model.[50] Numerous studies have demonstrated the reliability of M06-2X in accurately predicting the reaction energies of organic transformations.[51–58] The SMD solvation model has been widely used, and it is the best solvation model available in Gaussian. The frequency data were subsequently calculated at the same level of analysis. For total energy, the Def2-TZVP basis set,[59] coupled with the M06-2X functional, was utilized to perform single-point energy calculations. We will refer to these two sets of calculations as 6-31G(d)-Def2TZVP and PM7-Def2TZVP. All numerical values in the manuscript and ESI† are computed with the 6-31G(d)-Def2TZVP method. Generally, the reactions can be represented by the following equation:

$$XH_n \rightleftharpoons [XH_{n-n_p}]^{n_e} + n_p H^+ + n_e e^- \quad (10)$$

As previously discussed, the required H^+ is sourced from an aqueous solution, while e^- is derived from an electrode.

To assess the thermodynamics of the reaction, it is essential to determine the Gibbs free energy of each state involved in the process. The Gibbs free energies of the XH_n and $[XH_{n-n_p}]^{n_e}$ species can be readily analyzed, while the energetics of H^+ and e^- prove to be more complex. To address this issue, two following reactions are essential:

(i) The standard potential of the hydrogen electrode, as the reference electrode, is 0 V for the reaction written as

$$\frac{1}{2}H_2(g) \rightleftharpoons H^+(aq) + e^-. \quad (11)$$

(ii) An experimental pK_a, as a reference, is employed to capture the H^+(aq) Gibbs free energy. Herein, the formic

acid (HCOOH) dissociation reaction with a $pK_a^{ref.}$ of 3.77 is employed:[60]

$$HCOOH \rightarrow HCOO^- + H^+. \quad (12)$$

The logarithm of an acidity constant (K_a), represented by the pK_a value, is defined as follows:

$$pK_a = \frac{\Delta G_{PT}}{RT\ln(10)}. \quad (13)$$

Therefore, the reference Gibbs free energy change for reaction (12), denoted as $\Delta G_{PT}^{ref.}$, is calculated to be 0.224 eV.

The calculation of the Gibbs free energies for HCOOH and $HCOO^-$ can be easily performed. We determined that the Gibbs free energy of the solvated proton, denoted as $G_{H^+(aq)}$, is −11.798 eV. Referring back to eqn (11), we can compute that $G_{e^-} = -4.115$ eV. This value is based on computations defined above and it differs a bit from the IUPAC recommendation of −4.44 eV.

Subsequently, the obtained pK_a values need to be adjusted to address limitations inherent in the implicit solvation model used in our study,[37] as described below:

$$pK_a^{scaled} = 0.49 \times pK_a + 3.2 \quad (14)$$

As previously noted, no scaling formula has been established for the redox potentials of the ET and PET reactions that fit our computational setup. In the present study, we delineated these relationships.

4. Results and discussion

4.1. Scheme of square usage

To enhance the understanding of the calculations performed in this study, three distinct molecules were selected from various literature sources to evaluate the scheme of squares method, with comparisons made to experimental cyclic voltammetry (CV) data. In the first case, a single molecule was tested across a broad pH range experimentally, and the scheme of square calculations were performed at pH 7, pH 3, and pH 6, with results at pH 3 and pH 6 presented in the ESI.† In the second example, it was demonstrated that for molecules possessing a common backbone but varying positions of functional groups, some of the resulting compounds exhibited reversible behavior, while others did not. The third example highlighted that by modifying the applied potential, certain molecules could display reversible or irreversible characteristics.

4.1.1. Pyridinium-functionalized fluorenone. Li *et al.*[61] conducted detailed electrochemical surveys to elucidate the electrochemical mechanisms and structural transformations of OTDFL during its redox process. OTDFL, an acronym for 4-oxo-4,8,9,10-tetrahydro-7*a*,10*a*-diazacyclohepta[*def*]fluorene-7*a*,10*a*-diium, undergoes a two-step electron transfer involving distinct reaction mechanisms: initially ET followed by PET (Fig. 2(a)).

CV experiments were conducted using 1 mM OTDFL at various pH values. The redox potential for the initial redox process remained untouched at 0.16 V. In contrast, the redox potential for the subsequent redox process exhibited a downward shift from 0.12 V to −0.09 V as the pH increased from 3 to 7.

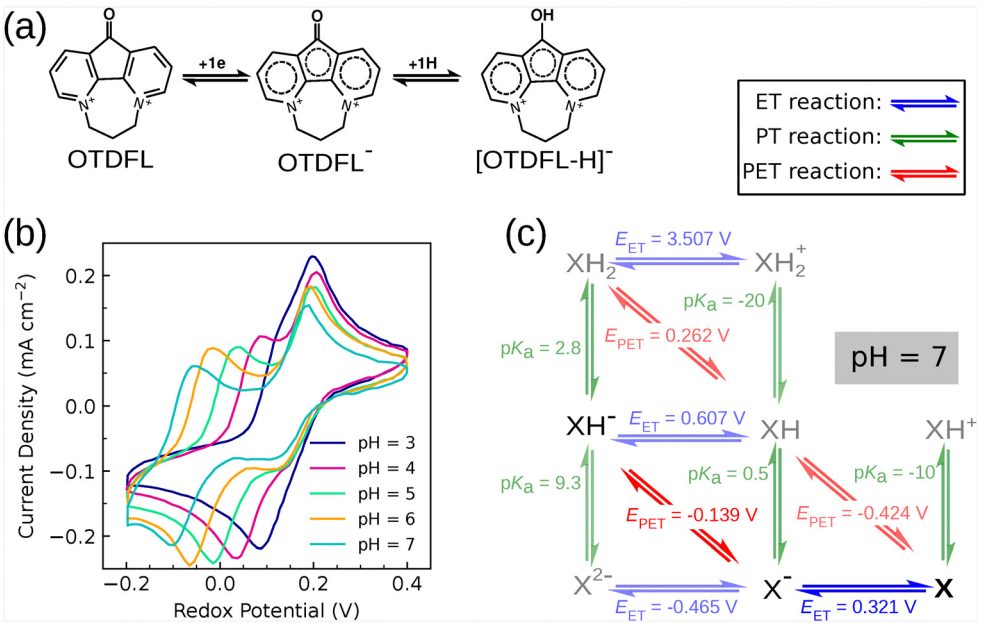

Fig. 2 (a) OTDFL participates in the ET and PET reactions during the reduction process. The oxygen atom in the ketone group is protonated. (b) Experimental cyclic voltammetry of OTDFL at different pH values from 3 to 7, taken from ref. 61. (c) The electrochemical scheme of the squares of OTDFL at pH 7. Vertical, horizontal, and diagonal arrows indicate the PT, ET, and PET reactions, respectively. PT is gauged by pK_a, whereas ET and PET are assessed by redox potentials in V, with PET potentials adjusted for the corresponding pH. The redox potential was referenced to the SHE. X represents the OTDFL compound.

This pH-dependent variation in the second redox process demonstrated a slope of 0.059 V per pH unit, indicative of a PET reaction (Fig. 2(b)). Consequently, a single peak with a slight shoulder evolves into a two-peak diagram, where the higher-potential-positioned peak is always fixed. All reactions were reversible.

Our scheme of squares (Fig. 2(c)) elucidates the following aspects of the redox reactions: (i) at all studied pH levels, OTDFL is first reduced through the ET reaction; (ii) the second electron transfer proceeds *via* a PET reaction, influencing the redox potential downshifts in response to the pH increases; (iii) the pathway X-to-X^{-}-to-XH^{-} remains consistent throughout the redox processes; (iv) at pH values less than 3 or greater than 9.3, redox reactions should not be reversible, terminating at XH_2 under acidic conditions or X^{2-} under alkaline conditions; (v) a minor discrepancy between experimental and computational redox potentials. This will be discussed in the Scaling redox potential section. Overall, we found good agreement between our calculations and the experimental results. The scheme of squares for pH values of 3 and 6 is found in Fig. S1 of the ESI.†

4.1.2. Fluorenone derivatives. Carboxylic acid (CA)-functionalized 9-fluorenone (FL) (see Fig. 3(a)) was tested under alkaline conditions (1 M KOH, pH = 14) with various positional configurations of CA.[62] The modified FLs were named based on their structural modifications: 9-fluorenone-1-carboxylic acid (FL-1CA), 9-fluorenone-2-carboxylic acid (FL-2CA), 9-fluorenone-3-carboxylic acid (FL-3CA), and 9-fluorenone-4-carboxylic acid (FL-4CA).

The electrochemical tests of FL-1CA, FL-2CA, and FL-4CA isomers are shown in Fig. 3(b). The FL-1CA compound underwent an irreversible reaction, whereas both FL-2CA and FL-4CA showed reversiblity. FL-1CA was reduced at a lower potential (≈ -0.812 V), indicating that it is more difficult to add an electron to it compared to FL-2CA and FL-4CA, which both had a similar reduction potential of approximately −0.69 V.

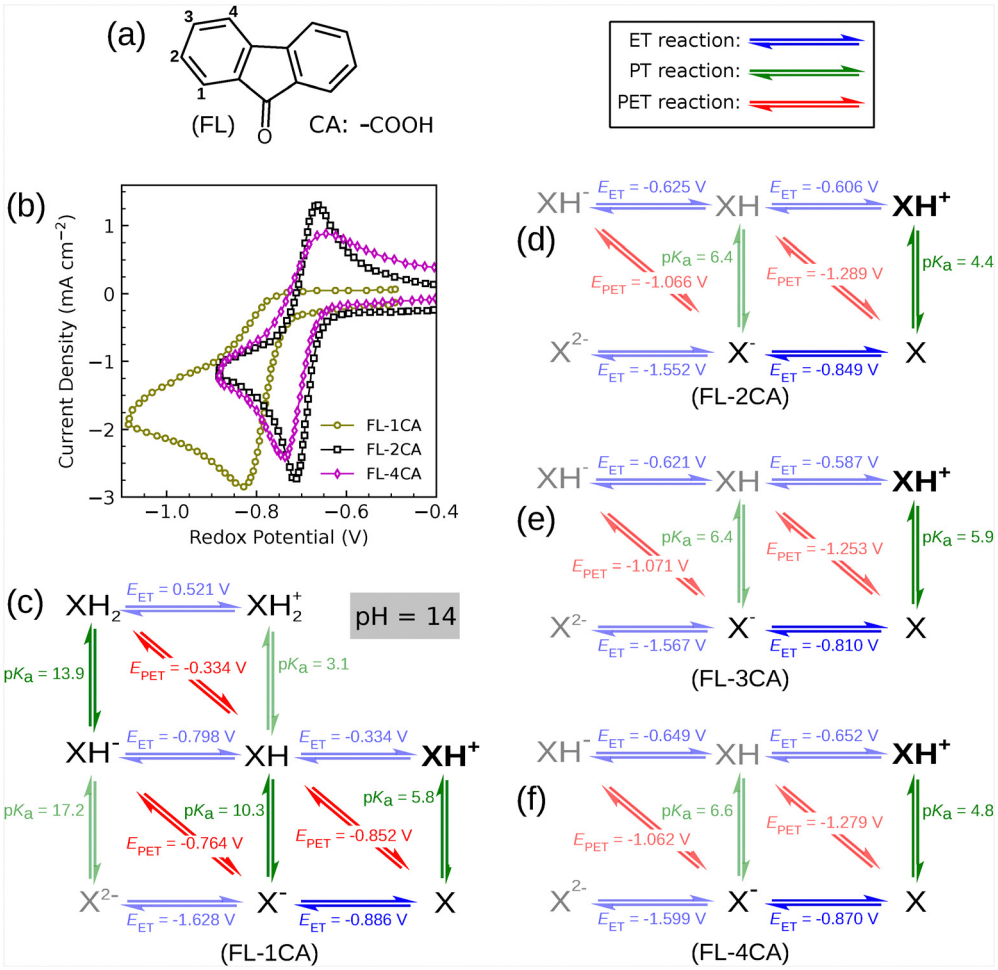

Fig. 3 (a) Graphical representation of 9-fluorenone (FL) with numbered functionalization sites. (b) Experimental cyclic voltammetry measurements were conducted on 10 mM solutions of carboxylic acid-functionalized FL compounds in 1 M KOH. The scan rate was set at 100 mV s^{-1}, as reported by Rodriguez *et al.*[62] The compounds are named FL-1CA, FL-2CA, and FL-4CA. (c)–(f) Electrochemical scheme of squares of 9-fluorenone derivatives (FL-*n*CA) including FL-1CA, FL-2CA, FL-3CA, and FL-4CA, at a pH of 14. Vertical, horizontal, and diagonal arrows indicate PT, ET, and PET reactions, respectively. PT is evaluated by pK_a, while ET and PET are assessed by redox potentials in V_{SHE}, with PET potentials adjusted for a pH of 14. XH^{+} represents the initial compound before equilibration (with COOH).

In experiments, a wider range of electrode potentials was used in the CV analysis of FL-1CA.

Adding the CA functional group not only increases the solubility of the compounds but also makes them more likely to undergo PT reactions during the stabilization process before starting CV measurements. FL-*n*CA derivatives can release H^+ depending on the pH of the environment. If the compound is more acidic than its surroundings, it acts as a proton donor, releasing hydrogen ions and transforming –COOH into $–COO^-$.

The calculated pK_a values for FL-1CA, FL-2CA, FL-3CA, and FL-4CA are 5.8, 4.4, 5.9, and 4.8, respectively, as shown in Fig. 3(c)–(f). The initial compound in each scheme is denoted as XH^+. Our calculated values indicate that these compounds are acidic and can immediately lose a proton under alkaline conditions. XH^+ is converted into X.

It is important to note that when –COOH is positioned next to the ketone group (C═O), it can form an internal hydrogen bond, significantly altering the electrochemical properties of the compound. As illustrated in Fig S2 (ESI†), the FL-1CA-H radical (XH form) is more stable than the other isomers due to the close proximity of the COOH hydrogen to the ketone oxygen. This increased stability reduces its acidic nature; compare the pK_a values of different isomers in their XH form. FL-1CA-H has a pK_a value of above 10, and the others are around 6.5. So it is less likely to be deprotonated. Overall, a planar structure is more favorable for all species in their XH radical form.

To analyze the CV diagrams, one should begin with the deprotonated form X. The redox reaction of FL-1CA is irreversible, exhibiting only one peak at a pH of 14. This indicates that it can be reduced but cannot be fully oxidized back to its original state. Fig. 3(c) shows that X participates in two distinct reactions at similar redox potentials: ET and PET. For example, if X undergoes a PET reaction and forms an XH radical, it can evolve into either XH^-, XH_2, or X^-. The first two pathways involve reduction, while the third pathway involves a deprotonation reaction. Conversely, if X forms X^- radicals *via* an ET reaction, the subsequent step is a PET reaction, in which XH^- equilibrates with XH_2. The predominant pathway is determined by the reaction kinetics. However, the presence of multiple reactive species in the solution not only reduces the oxidation rate but may also increase the likelihood of side reactions.

The placement of the –COOH group at sites 2, 3, and 4 completely changed the reaction mechanism. Only one reaction can occur: the formation of X^- from X. The X-to-XH pathway is blocked because at a pH of 14 it is hard to source H^+. Applying more potential could push the PET reaction to occur in the range of −1.062 to −1.071 V. In the experiment, the applied potential was increased to −0.9 V; therefore, only one peak is expected.

4.1.3. Benzoylpyridinium. In an experiment conducted by Sevov *et al.*,[63] electron transfer occurred *via* the decoupled ET and PET reactions. The investigation focused on 1-benzyl-4-methyl-pyridinium (BenPy) (concentration 10 mM) within a 1 M NaCl aqueous solution (Fig. 4(a)).

The CV analysis exhibited two peaks at −0.63 and −0.73 V, with poor reversibility (Fig. 4(b), green symbols). Nonetheless, adhering to a conservative CV sweep limit of −0.73 V prevented adverse second reduction, revealing a reversible diagram (Fig. 4(b), blue symbols). Furthermore, during the bulk electrolysis

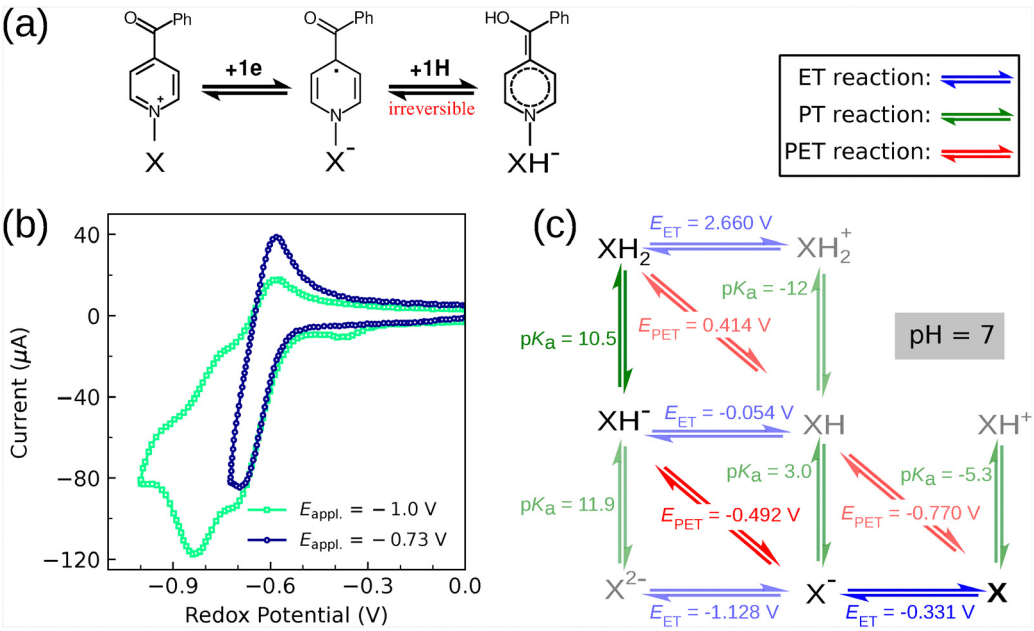

Fig. 4 BenPy participates in the ET and PET reactions during the reduction process when a potential of up to −1 V is applied. (b) Experimental cyclic voltammetry of BenPy at different applied potentials of −0.73 and −1 V *versus* the SHE, taken from ref. 63. (c) The electrochemical scheme of the squares of BenPy at pH 7. Vertical, horizontal, and diagonal arrows indicate the PT, ET, and PET reactions, respectively. PT is gauged by pK_a, whereas ET and PET are assessed by redox potentials in V, with PET potentials adjusted for the corresponding pH. The redox potential was referenced to the SHE. X represents the BenPy.

experiments, the dissolution of compound X^- in 1 M KOH (pH ≈ 14) at room temperature without the application of any potential demonstrated no reactivity. Conversely, dissolving in a 0.1 M HCl (pH ≈ 1) aqueous solution resulted in nearly instantaneous bleaching of the purple color of the radical.

Using the electrochemical scheme (Fig. 4(c)), starting with species X at a pH of 7, a potential of −0.331 V is required to initiate the first ET reaction. Subsequently, the second electron is transferred at −0.492 V through a PET mechanism, converting X^- to XH^-. Because this reaction is influenced by the pH, the redox potential becomes more negative as the pH increases. Eventually, compound XH^-, which displays stronger basic characteristics than the medium, can be protonated, forming species XH_2. The deprotonation reaction is no longer favored, and the system remains trapped in this state, unless the applied potential facilitates its reversibility through a PET reaction.

Given that the PET oxidation reaction (XH_2 to XH path) is thermodynamically unfavorable, a much higher positive electrode potential is required. A comparison of the reduction and oxidation potentials highlights a significant overpotential, indicating that the reaction proceeds sluggishly and ultimately irreversibly.

Similar to the experiment, our calculations revealed a gap between the redox potentials of the ET (from X to X^-) and PET (from X^- to XH^-) reactions. However, similar to the previous example, the calculated potentials were overestimated compared to the experimental values. Thus, calibration of the calculated values against the experimental data becomes useful.

Additionally, the bulk electrolysis results are supported by a pK_a value of 3 for the XH-to-X^- deprotonation reaction. This indicates that at a pH of >3, X^- will remain stable in the solution, while at lower pH values, it will accept a proton and will be converted into XH. This explains the observed color change of the solution.

4.2. Scaling redox potentials

In addition to the three examples above, we have investigated 60 additional molecules and compared them to experimental CV analysis collecting data from the aqueous organic redox flow battery[64–66] literature. For each case, we examined the reaction pathway and collected the corresponding redox potential quantities. The scheme of squares sheds light on which the ET or PET reaction corresponds to the observed current peak (further details are provided in Sections V and VI of the ESI†). The molecules considered for this purpose include quinones,[67] phthalazines,[68] phenazines,[69] benzidines,[70] TEMPO,[71] and viologens.[72] To our knowledge, this is the broadest comparison of the computational and experimental scheme of squares results.

For the PET reactions, the redox potentials were adjusted to a pH of 0 using the Nernst equation (eqn (9)). All experiments were performed at room temperature. In total, 60 and 36 samples were used to establish linear scaling relationships for ET and PET, respectively.

To calculate the scheme of squares, we considered two computational setups. First, a more precise M062X-Def2TZVP setup was used which is suitable for the single-case studies, due to its high computational cost. Second, a PM7-Def2TZVP combination was employed, which is crucial for large database generation, as we did previously.[30]

As shown in Fig. 5, our computational setup demonstrated notable accuracy, particularly in the realm of ET reactions. Here, we report a R^2 value of 0.98 and a scaling relationship of $0.91E^0_{\mathrm{dft}} - 0.12$. Our PET model has a small intercept value of 0.04 V. With a slope of 0.85, the calculations slightly overestimates the redox potential. The R^2 value of 0.89 indicates a good level of reliability. Comparing to the fast calculations (see Fig. S3, ESI†), where a different method was used for geometry optimization (DFT *vs.* semiempirical method), we observed only slight variations in the coefficients of the linear model. This outcome is consistent with the findings reported in ref. 37 regarding pK_a. The values reported earlier in this paper are unscaled but applying fitting relationships for the potentials, we generally find closer agreement with the experiments.

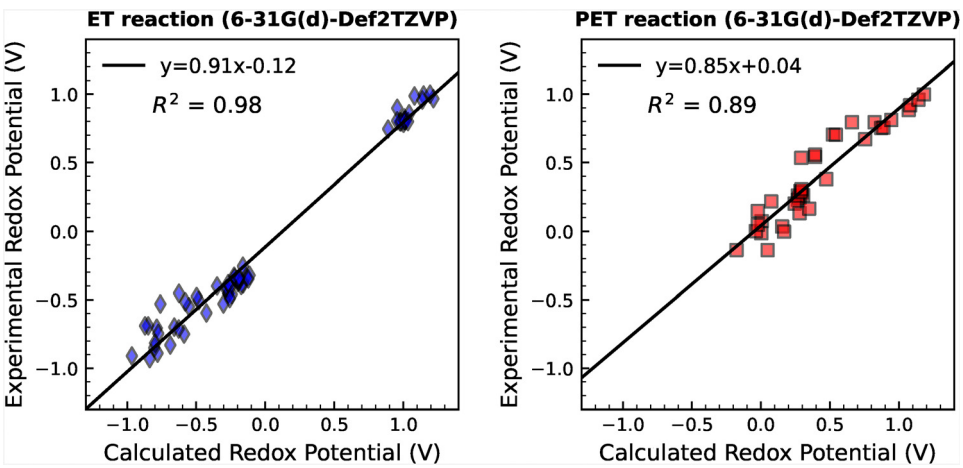

Fig. 5 Scaling of the calculated redox potentials of the ET and PET reactions against the experimental data. Calculations were performed using the 6-31G(d)-Def2TZVP computational setup. Each subplot includes the linear regression model formula along with the coefficient of determination (R^2).

We see that the good scaling relationship is strong proof that our simple computational approach has good predictive power. The experimental systems are complex, with real electrodes, done in various pH values, possible concentrations and transport effects, whereas we model only one molecule with the continuum solvation model, and still the agreement is good on a large set of molecules. More detailed models for electrochemical reactions can be used[23,73] but they are very time consuming and unsuitable for molecular screening. The current scaling results are very encouraging but if this computational approach is used for quite different molecules than studied here, careful comparisons to experimental results are needed.

The molecules presented in the ESI† provide a lot of details of the ET, PT and PET reactions of a rather broad range of molecules. With compounds 1–36, the agreement with experiments is good. Compounds A–F are more challenging and some results are not in good agreement. This is partly due to the complexity of the molecules and there can be other reactions, than the proton reactions we studied here, which affect the measured redox potentials.

5. Conclusions

Separating the PET reaction into distinct ET and PT reactions is experimentally possible but rather time consuming whereas it is computationally easy. With the computational setup in this work, the virtual screening of redox potentials of a large set of organic molecules is feasible. We can perform the electrochemical scheme of square computations and predict the experimental redox potentials at given pH values. The observed good scaling relationships with a quite large amount of molecules demonstrate that the computational procedure is reliable. These computations will also provide information on the reaction type (ET, PT, or PET). The computational approach can explain, in some cases, the irreversibility observed in cyclic voltammetry. Our approach is limited to irreversibility caused by the protonation states. Overall, the computations will provide a lot of information on electrochemical ET, PT, and PET-type reactions. This is useful when searching molecules with desired redox potentials at certain pH. These findings can be applied to redox reactions and acid–base reactions across a wide range of scientific fields, including energy storage, medicine, and synthetic chemistry.

Author contributions

Amir Mahdian: investigation, software, methodology, formal analysis, data collection and writing. Arsalan Hashemi: conceptualization, software, data curation, and writing – review and editing. Kari Laasonen: conceptualization, resources, funding acquisition, project administration, supervision, and writing – review and editing.

Conflicts of interest

There are no conflicts to declare.

Data availability

Detailed molecular structures and computational inputs are available for download from the Zenodo database (**https://zenodo.org/records/12736686**).

Acknowledgements

This project has received funding from the European Union – NextGenerationEU instrument *via* Research Council Finland under grant number 348327. We thank the CSC – IT Center for Science for computational resources.

References

1 X. Chen, X. Xie, P. Ruan, S. Liang, W.-Y. Wong and G. Fang, *ACS Energy Lett.*, 2024, **9**, 2037–2056.
2 R. Feng, Y. Chen, X. Zhang, B. J. Rousseau, P. Gao, P. Chen, S. T. Mergelsberg, L. Zhong, A. Hollas, Y. Liang, V. Murugesan, Q. Huang, E. Walter, S. Hammes-Schiffer, Y. Shao and W. Wang, *Joule*, 2023, **7**, 1609–1622.
3 T. V. Sawant, C. S. Yim, T. J. Henry, D. M. Miller and J. R. McKone, *Joule*, 2021, **5**, 360–378.
4 S. Srinivasan, *Fuel Cells: From Fundamentals to Applications*, Springer Science & Business Media, 2006.
5 W. Mook, M. Aroua and G. Issabayeva, *Renewable Sustainable Energy Rev.*, 2014, **38**, 36–46.
6 S. Grigoriev, V. Fateev, D. Bessarabov and P. Millet, *Int. J. Hydrogen Energy*, 2020, **45**, 26036–26058.
7 M. Seralathan and S. Rangarajan, *J. Electroanal. Chem.*, 1985, **191**, 209–228.
8 C. Wiberg, M. Busch, L. Evenäs and E. Ahlberg, *Electrochim. Acta*, 2021, **367**, 137480.
9 Q. Xu and T. S. Zhao, *Prog. Energy Combust. Sci.*, 2015, **49**, 40–58.
10 G. L. Soloveichik, *Chem. Rev.*, 2015, **115**, 11533–11558.
11 A. Orita, M. Verde, M. Sakai and Y. Meng, *J. Power Sources*, 2016, **321**, 126–134.
12 M. M. Cooper, H. Kouyoumdjian and S. M. Underwood, *J. Chem. Educ.*, 2016, **93**, 1703–1712.
13 T. Ree, *J. Chem. Educ.*, 1971, **48**, 467.
14 M. Ingelsson, N. Yasri and E. P. L. Roberts, *Water Res.*, 2020, **187**, 116433.
15 O. Nolte, P. Rohland, N. Ueberschaar, M. D. Hager and U. S. Schubert, *J. Power Sources*, 2022, **525**, 230996.
16 M. Pourbaix, *Corrosion*, 1950, **6**, 395–404.
17 G. A. Mabbott, *J. Chem. Educ.*, 1983, **60**, 697.
18 N. Elgrishi, K. J. Rountree, B. D. McCarthy, E. S. Rountree, T. T. Eisenhart and J. L. Dempsey, *J. Chem. Educ.*, 2018, **95**, 197–206.
19 P. Chooto, *Voltammetry*, IntechOpen, 2019, p. 1.
20 N. Navashree and P. Parthasarathy, *Mater. Today: Proc.*, 2023, DOI: **10.1016/j.matpr.2023.05.175**.
21 G. Korotcenkov, S. D. Han and J. R. Stetter, *Chem. Rev.*, 2009, **109**, 1402–1433.

22 J. J. Van Benschoten, J. Y. Lewis, W. R. Heineman, D. A. Roston and P. T. Kissinger, *J. Chem. Educ.*, 1983, **60**, 772.
23 A. Hashemi, P. Peljo and K. Laasonen, *J. Phys. Chem. C*, 2023, **127**, 3398–3407.
24 J. Kim and H. Park, *Renewable Energy*, 2019, **138**, 284–291.
25 V. Muralidharan, S. Jayasubramaniyan and H.-W. Lee, *EES Catal.*, 2024, **2**, 522–544.
26 E. L. Lebeau, R. A. Binstead and T. J. Meyer, *J. Am. Chem. Soc.*, 2001, **123**, 10535–10544.
27 S. Hammes-Schiffer, *Chem. Rev.*, 2010, **110**, 6937–6938.
28 E. Laviron and L. Roullier, *J. Electroanal. Chem.*, 1985, **186**, 1–15.
29 M. Okubo, K. Kawai, Z. Ma and A. Yamada, *Acc. Mater. Res.*, 2022, **3**, 33–41.
30 A. Hashemi, R. Khakpour, A. Mahdian, M. Busch, P. Peljo and K. Laasonen, *Digital Discovery*, 2023, **2**, 1565–1576.
31 K. Burke, *J. Chem. Phys.*, 2012, **136**, 150901.
32 F. Giustino, *Materials Modelling Using Density Functional Theory: Properties and Predictions*, Oxford University Press, 2014.
33 K. Mathew, R. Sundararaman, K. Letchworth-Weaver, T. Arias and R. G. Hennig, *J. Chem. Phys.*, 2014, **140**, 084106.
34 J. Rossmeisl, Z.-W. Qu, H. Zhu, G.-J. Kroes and J. Nørskov, *J. Electroanal. Chem.*, 2007, **607**, 83–89.
35 M. Bursch, J.-M. Mewes, A. Hansen and S. Grimme, *Angew. Chem., Int. Ed.*, 2022, **61**, e202205735.
36 R. P. Fornari and P. de Silva, *Molecules*, 2021, **26**, 3978.
37 M. Busch, E. Ahlberg, E. Ahlberg and K. Laasonen, *ACS Omega*, 2022, **7**, 17369–17383.
38 A. V. Marenich, C. J. Cramer and D. G. Truhlar, *J. Phys. Chem. B*, 2009, **113**, 6378–6396.
39 A. Klamt, F. Eckert, M. Diedenhofen and M. E. Beck, *J. Phys. Chem. A*, 2003, **107**, 9380–9386.
40 T. N. Brown and N. Mora-Diez, *J. Phys. Chem. B*, 2006, **110**, 9270–9279.
41 L. Tomaník, L. Rulíšek and P. Slavíček, *J. Chem. Theory Comput.*, 2023, **19**, 1014–1022.
42 A. Hamza, F. B. Nemeth, d Madarasz, A. Nechaev, P. M. Pihko, P. Peljo and I. Papai, *Chem. – Eur. J.*, 2023, **29**, e202300996.
43 A. R. McNeill, S. E. Bodman, A. M. Burney, C. D. Hughes and D. L. Crittenden, *J. Phys. Chem. C*, 2020, **124**, 24105–24114.
44 M. Namazian, C. Y. Lin and M. L. Coote, *J. Chem. Theory Comput.*, 2010, **6**, 2721–2725.
45 A. J. Bard, L. R. Faulkner and H. S. White, *Electrochemical Methods: Fundamentals and Applications*, John Wiley & Sons, 2022.
46 D. Pavlov, *Lead-Acid Batteries: Science and Technology: A Handbook of Lead-Acid Battery Technology and Its Influence on the Product*, Elsevier Science Limited, 2011.
47 M. J. Frisch, G. W. Trucks, H. B. Schlegel, G. E. Scuseria, M. A. Robb, J. R. Cheeseman, G. Scalmani, V. Barone, G. A. Petersson, H. Nakatsuji, X. Li, M. Caricato, A. V. Marenich, J. Bloino, B. G. Janesko, R. Gomperts, B. Mennucci, H. P. Hratchian, J. V. Ortiz, A. F. Izmaylov, J. L. Sonnenberg, D. Williams-Young, F. Ding, F. Lipparini, F. Egidi, J. Goings, B. Peng, A. Petrone, T. Henderson, D. Ranasinghe, V. G. Zakrzewski, J. Gao, N. Rega, G. Zheng, W. Liang, M. Hada, M. Ehara, K. Toyota, R. Fukuda, J. Hasegawa, M. Ishida, T. Nakajima, Y. Honda, O. Kitao, H. Nakai, T. Vreven, K. Throssell, J. A. J. Montgomery, J. E. Peralta, F. Ogliaro, M. J. Bearpark, J. J. Heyd, E. N. Brothers, K. N. Kudin, V. N. Staroverov, T. A. Keith, R. Kobayashi, J. Normand, K. Raghavachari, A. P. Rendell, J. C. Burant, S. S. Iyengar, J. Tomasi, M. Cossi, J. M. Millam, M. Klene, C. Adamo, R. Cammi, J. W. Ochterski, R. L. Martin, K. Morokuma, O. Farkas, J. B. Foresman and D. J. Fox, *Gaussian 16 Revision C.01*, 2016, Gaussian Inc., Wallingford CT.
48 P. Hariharan and J. Pople, *Theor. Chim. Acta*, 1973, **28**, 213–222.
49 J. J. Stewart, *J. Mol. Model.*, 2013, **19**, 1–32.
50 A. V. Marenich, C. J. Cramer and D. G. Truhlar, *J. Phys. Chem. B*, 2009, **113**, 6378–6396.
51 K. Farshadfar and K. Laasonen, *ACS Catal.*, 2024, **14**, 14486–14496.
52 T. Zheng, J. Ma, H. Chen, H. Jiang, S. Lu, Z. Shi, F. Liu, K. N. Houk and Y. Liang, *J. Am. Chem. Soc.*, 2024, **146**, 25058–25066.
53 C. R. Travis, R. G. Dumais, J. W. Treacy, K. M. Kean, K. N. Houk and M. L. Waters, *J. Am. Chem. Soc.*, 2024, **146**, 20678–20684.
54 P. Ma, D. Svatunek, Z. Zhu, D. L. Boger, X.-H. Duan and K. N. Houk, *J. Am. Chem. Soc.*, 2024, **146**, 18706–18713.
55 R. J. Monsky, Y. Li, K. N. Houk and W. R. Dichtel, *J. Am. Chem. Soc.*, 2024, **146**, 17150–17157.
56 M. Duan, Q. Shao, Q. Zhou, P. S. Baran and K. N. Houk, *Nat. Commun.*, 2024, **15**, 4630.
57 H. Tian, W. Lee, Y. Li, M. J. Dweck, A. Mendoza, P. G. Harran and K. N. Houk, *J. Am. Chem. Soc.*, 2024, **146**, 5375–5382.
58 S. Dutta, Y.-L. Lu, J. E. Erchinger, H. Shao, E. Studer, F. Schäfer, H. Wang, D. Rana, C. G. Daniliuc and K. N. Houk, *et al.*, *J. Am. Chem. Soc.*, 2024, **146**, 5232–5241.
59 F. Weigend, F. Furche and R. Ahlrichs, *J. Chem. Phys.*, 2003, **119**, 12753–12762.
60 J. Ho and M. L. Coote, *Theor. Chem. Acc.*, 2009, **125**, 3.
61 W. Li, J. Li, X. Yuan, Z. Xiang, Z. Liang and Z. Fu, *J. Mater. Chem. A*, 2023, **11**, 19308–19311.
62 J. Rodriguez, C. Niemet and L. D. Pozzo, *ECS Trans.*, 2019, **89**, 49.
63 C. S. Sevov, K. H. Hendriks and M. S. Sanford, *J. Phys. Chem. C*, 2017, **121**, 24376–24380.
64 R. Chen, *ChemElectroChem*, 2019, **6**, 603–612.
65 S. Gentil, D. Reynard and H. H. Girault, *Curr. Opin. Electrochem.*, 2020, **21**, 7–13.
66 C. Flox, C. Zhang and Y. Li, *Curr. Opin. Chem. Eng.*, 2023, **39**, 100880.
67 R. H. R. H. Thomson, *Naturally Occurring Quinones*, Elsevier, 2012.

68 N. R. Patel, *Phthalazines*, John Wiley & Sons, Ltd, 1973, ch. II, pp. 323–760.
69 J. B. Laursen and J. Nielsen, *Chem. Rev.*, 2004, **104**, 1663–1686.
70 T. J. Haley, *Clin. Toxicol.*, 1975, **8**, 13–42.
71 T. Vogler and A. Studer, *Synthesis*, 2008, 1979–1993.
72 C. L. Bird and A. T. Kuhn, *Chem. Soc. Rev.*, 1981, **10**, 49–82.
73 R. Kronberg and K. Laasonen, *ACS Catal.*, 2021, **22**, 8062–8078.